Research Article Vol. 7, No. 7 / July 2020 / Optica 755

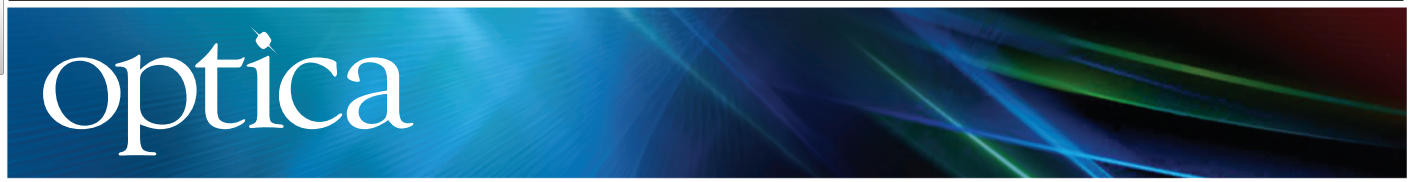

SPAD-based asynchronous-readout array detectors for image-scanning microscopy

Mauro Buttafava,[1] Federica Villa,[1] Marco Castello,[2] Giorgio Tortarolo,[2,3] Enrico Conca,[1] Mirko Sanzaro,[1] Simonluca Piazza,[4] Paolo Bianchini,[4] Alberto Diaspro,[4,5] Franco Zappa,[1] Giuseppe Vicidomini,[2] and Alberto Tosi[1,*]

[1]Dipartimento di Elettronica, Informazione e Bioingegneria, Politecnico di Milano, Milano, Italy
[2]Molecular Microscopy and Spectroscopy, Istituto Italiano di Tecnologia, Genova, Italy
[3]Dipartimento di Informatica, Bioingegneria, Robotica e Ingegneria dei Sistemi, Università di Genova, Genova, Italy
[4]Nanoscopy and NIC@IIT, Istituto Italiano di Tecnologia, Genova, Italy
[5]Dipartimento di Fisica, Università di Genova, Genova, Italy
*Corresponding author: alberto.tosi@polimi.it

Received 10 March 2020; revised 1 June 2020; accepted 5 June 2020 (Doc. ID 391726); published 1 July 2020

Fluorescence microscopy and derived techniques are continuously looking for photodetectors able to guarantee increased sensitivity, high spatial and temporal resolution, and ease of integration into modern microscopy architectures. Recent advances in single-photon avalanche diodes (SPADs) fabricated with industry-standard microelectronic processes allow the development of new detection systems tailored to address the requirements of advanced imaging techniques (such as image-scanning microscopy). To this aim, we present the complete design and characterization of two bidimensional SPAD arrays composed of 25 fully independent and asynchronously operated pixels, both having fill factor of about 50% and specifically designed for being integrated into existing laser scanning microscopes. We used two different microelectronics technologies to fabricate our detectors: the first technology exhibiting very low noise (roughly 200 dark counts per second at room temperature) and the second one showing enhanced detection efficiency (more than 60% at a wavelength of 500 nm). Starting from the silicon-level device structures and moving towards the in-pixel and readout electronics description, we present performance assessments and comparisons between the two detectors. Images of a biological sample acquired after their integration into our custom image-scanning microscope finally demonstrate their exquisite on-field performance in terms of spatial resolution and contrast enhancement. We envisage that this work can trigger the development of a new class of SPAD-based detector arrays able to substitute the typical single-element sensor used in fluorescence laser scanning microscopy.

https://doi.org/10.1364/OPTICA.391726

1. INTRODUCTION

Since the early 1990s, single-photon detectors started to play a growing role in scientific and industrial environments, and microscopy was one of the first applications taking advantage of the extremely high sensitivity of these devices. Confocal laser-scanning microscopy (CLSM) [1], fluorescence lifetime image microscopy (FLIM) [2], fluorescence correlation spectroscopy (FCS) [3], down to modern super-resolution techniques, such as stimulated emission-depletion (STED) [4,5] and image-scanning microscopy (ISM) [6,7], are only some of the applications currently enabled by single-photon detectors.

Vacuum-based devices, like photomultiplier tubes (PMT) and microchannel plates (MCP), historically played a leading role in the field, despite limitations like fragility, intrinsic deterioration with usage, high cost, bulkiness, and operation complexity. This was essentially due to advantages like large active area and high measurement dynamic range.

More recently, microelectronic single-photon detectors like single-photon avalanche diodes (SPADs) are gaining importance in microscopy applications thanks to their great reliability, robustness, ease of operation, high detection efficiency, low timing jitter, and their integrability with read-out circuits, allowing for the development of arrays. SPADs are essentially $p-n$ junctions reversed-biased above their breakdown voltage [8,9], where absorbed photons can generate a self-sustaining carrier multiplication process (avalanche), which eventually translates into a macroscopic current that can be easily detected by an external discriminator circuit. Silicon SPADs are used to detect photons in the visible wavelength range, from 400 to 1000 nm, while SPADs based on III-V compound materials (like InGaAs/InP) are useful to detect signals in the near-infrared region (from 900 to 1700 nm) [10].

Single-pixel silicon SPADs can be divided into two categories, according to their internal device structure: i) the so-called *thick SPADs* [11,12] are commonly employed in fluorescence microscopes thanks to their very good photon detection efficiency (PDE), which can be as high as 70% at 780 nm, but are characterized by a poorer temporal resolution [350 ps full width at half-maximum (FWHM)] with respect to the so-called *thin SPADs* [13–15], which can reach temporal resolutions down to 30 ps at the expense of a lower PDE. Besides the higher temporal resolution (of fundamental importance in time-resolved microscopy applications like FLIM), the real strength of thin SPADs is the compatibility with microelectronic circuits, which allows the integration of dedicated electronics into the same silicon chip [9] for creating 1D and 2D arrays of detectors, effectively implementing single-photon imagers with photon-timing capability.

A wide variety of monolithic SPAD array implementations can be found in the literature [16]. Suitable fabrication technologies include CMOS process nodes down to 40 nm [17], as well as lower-density but more consolidated nodes, e.g., 0.35 μm [18]. New opportunities are also offered by the recently explored 3D-stacked imagers, employing two different technologies for the detector array and the front-end electronics [19,20]. Pixel number can be as high as 1 MP [21], and in-pixel electronics can include up/down counters [22], time-to-digital converters [17,23,24], time gating [24], and coincidence detection circuits [24,25]. However, the combination of high pixel number and embedded processing circuits has the drawback of generating massive quantity of data that needs to be transferred outside the chip. Image readout is then usually implemented using serial communication protocols and is based on frames (i.e., data related to the entire imager is downloaded periodically, independently of the number of triggered pixels). The frame rate is usually limited to few hundreds of kilo-frames/s, also depending onto the communication interface used to transfer data from the detection system to the PC (typically USB 2.0 or 3.0). This approach can be a bottleneck in applications not requiring high pixel number, but rather fast readout speed and the possibility to independently address each pixel, such as ISM.

In a nutshell, image-scanning microscopy requires collection of the image of the excitation/detection region for each scanning position of the sample. Since the excitation region is diffraction limited, its size is typically in the range of few hundreds of nanometers (the size reduces when ISM is combined with STED microscopy [26]) and the pixel dwell time is in the microseconds range (a few tens of nanoseconds when ISM is combined with resonant scanners). Thus, it is clear the importance of having a detector array with a limited number of pixels but with asynchronous readout (no frame rate). The lack of a detector having these requirements was the major reason for the delay in the practical implementation of ISM. Indeed, ISM has been proposed in the 1980s [27,28], offering an approach to solve one of the most critical aspects of CLSM (effectively introducing it in the pool of super-resolution techniques), but it took more than 30 years to see a versatile implementation of this idea. In fact, CLSM can be considered a super-resolution microscopy technique, allowing the diffraction barrier to be overcome by a factor of $\sqrt{2}$ as defined by the FWHM of the point spread function (PSF). In practice, however, this improvement can be obtained only by reducing the diameter of the confocal pinhole, but this translates into a significant reduction of the signal-to-noise ratio (SNR) of the resulting images.

Since in ISM the single-pixel photodetector is replaced by an imaging detector and the pinhole is removed (or opened to a size greater than 1 Airy unit), each pixel/element of the detector effectively acts a virtual pinhole, but all the light reaching the image plane is collected. The final ISM image is then obtained by computationally combining the information contained in the 2D dataset of the acquired images [29,30], i.e., after each scanning the microscope produces one confocal image for every pixel/element of the detector array (the so-called scanned images). The most important aspect of ISM is the increase of the detected signal level compared to simple confocal imaging (thus allowing imaging with lower excitation power), while at the same time slightly improving upon the confocal resolution limit.

ISM implementations have been demonstrated with conventional cameras [6], at the expense of a low imaging speed (due to the limited camera frame rate) or with *optomechanical* implementations [31–34], which have the drawback of a substantial modification of the microscope structure. Recently, the imaging speed limit was addressed by the *Airyscan* implementation of CLSM (*Carl Zeiss AG*) [35], for which a 2D bundle of optical fibers is coupled to a linear array of GaAsP PMTs. However, this solution still hinders the temporal information related to photon arrivals (thus preventing the implementation of FLIM and similar techniques) and exhibits some of the typical restrictions of vacuum-based detectors (like fragility and high cost).

It is thus clear that designing a small SPAD array with picosecond timing ability and fully independent pixel operation and readout would be a very effective solution to overcome all the above limitations, and to implement faster and more flexible image-scanning microscopes.

In this work, we describe design and characterization of two five-by-five SPAD arrays, fabricated in two different technologies and specifically tailored for ISM applications. Theoretical studies show that this relatively small number of pixels (i.e., 25) is sufficient for practical applications, since a higher number of elements would provide only a marginal resolution gain [30]. For both implementations, in the following sections we will describe the SPAD structures, the overall imager architectures, their optical and electrical characterization, and an example of ISM used for imaging the convoluted tubulin network of a human cell.

2. SENSOR DESIGN

The microelectronic fabrication processes used for our asynchronous-readout image sensors are: i) a 0.35 μm high-voltage CMOS technology (0.35 μm HVCMOS) [18] and ii) a 0.16 μm bipolar-CMOS-DMOS technology (0.16 μm BCD) [36]. Sensor architecture and geometry remain the same, but the detection performance is strongly affected by the chosen technology. In detail, devices developed using our 0.35 μm HCMOS are characterized by best-in-class dark-count noise, while the 0.16 μm BCD SPADs feature bespoke dopant implants for enhanced detection efficiency.

A. SPAD Fabrication Technologies

A simplified cross section of our SPADs fabricated using the 0.35 μm HVCMOS technology is shown in Fig. 1A. A high-voltage *n* well isolates the device from the *p*-type substrate. Shallow *p*+ and *n*+ implants are the anode and cathode contacts of the device, respectively. A further low-energy *n*-type enrichment implant defines the high field multiplication region (i.e., the SPAD

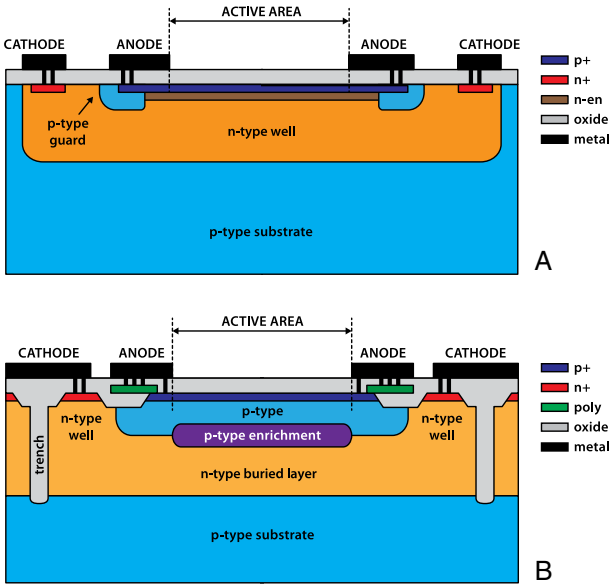

Fig. 1. Simplified cross section of the SPAD inside each individual imaging pixel, fabricated using the (A) 0.35 μm HVCMOS and (B) 0.16 μm BCD SPAD technology. Both fabrication processes are industry standards and allow for the integration of in-pixel electronics (not shown in the cross section). Features in the images are not in scale.

active area). Finally, a *p*-type implantation is used as a guard ring to suppress premature edge breakdown effects. Although a common cathode *n* well could be shared by all SPADs of the array enhancing the fill factor, the SPAD pixels reported in this paper are isolated from one another to reduce electrical crosstalk. In this device structure the avalanche is mainly triggered by holes, which have an impact ionization coefficient lower than electrons and thus lead to a lower PDE.

The simplified cross section of the 0.16 μm BCD SPAD [36] is shown in Fig. 1B. Each device is fully enclosed in a double-well pocket, formed by a *n*-type buried layer, for isolation from the *p*-type substrate, and a heavily doped *n*-type well, which provides a low resistance path to the cathode contact. This fabrication technology also features deep trenches, which here are exploited for electrical and optical isolation between pixels. As in the 0.35 μm HVCMOS SPAD, a bespoke enrichment implant defines the avalanche region. However, in this case, a high-energy *p*-type implant is used. As a result, the avalanche region has been moved towards the *n*-type buried layer, and the avalanche current is mainly triggered by electrons.

B. Array Geometry

To allow for fully asynchronous and independent readout from the image sensor, while maintaining the maximum flexibility in data processing, the output signal from each pixel is routed to a digital output pad. Each photon detection in the *N*th pixel is marked by the trailing edge of a voltage pulse onto the *N*th output pad, with a time uncertainty (jitter) lower than a few tens of picoseconds. The drawback is the growing complexity when increasing the pixel number, due to longer electrical connections and the higher pin count. The square geometry of five-by-five pixels was chosen as a compromise between spatial resolution and device complexity, always keeping in mind the target ISM application, while different implementations available in the literature make use of hexagonal patterns [37]. Table 1 summarizes the geometry details of the designed sensors.

Table 1. SPAD Array Sensors' Single-Pixel Geometry Details

	0.35 μm HVCMOS	0.16 μm BCD
Pixel side length	50 μm	57 μm
Pixel corner radius	5 μm	5 μm
Pixel pitch	75 μm	75 μm
Array fill factor	44%	57.5%

The pixel active area is square with rounded corners, in order to maximize the array fill factor (i.e., the ratio between the photosensitive area and the overall silicon area). A 5 μm curvature radius is sufficient to avoid premature edge-breakdown effects due to electrical field peaking at corners. The pixel pitch (i.e., distance from center to center) is 75 μm, with a side length of 50 μm for the 0.35 μm HVCMOS device (leading to a fill factor of about 44%), which is increased to 57 μm for the 0.16 μm BCD device, thanks to the smaller minimum feature size of this technology (which allows for a smaller gap between pixels, leading to a fill factor of around 57.5%). A detailed view of the photosensitive section of both devices is shown in Figs. 2A and 2B. The overall image sensors have total dimensions of $2.2 \times 2.4\ \text{mm}^2$ (mainly limited by the output pads) for the 0.35 μm HVCMOS one and $1.3 \times 1.2\ \text{mm}^2$ (owing to the smaller pad pitch) for the 0.16 μm BCD one. In this context, it is important to highlight that having a relatively small total active area (i.e. $\sim 350 \times 350\ \mu\text{m}^2$) is convenient from an optical point of view, since having a projected size of the SPAD array on the sample plane of ~1 Airy unit requires adding only a relatively small extra magnification to a conventional laser scanning architecture.

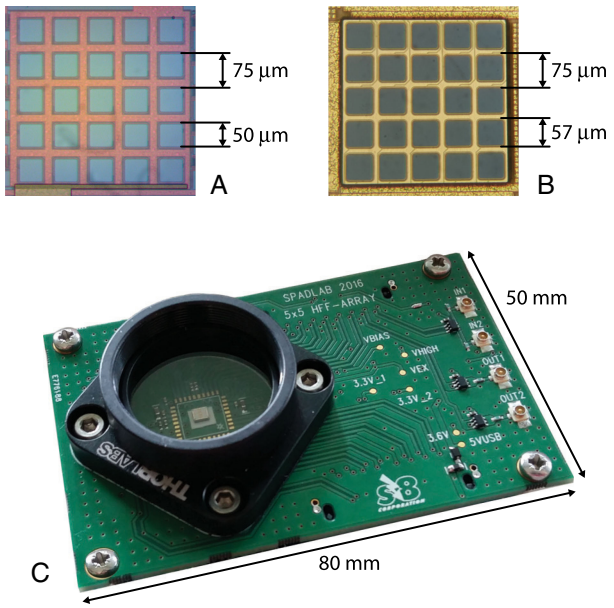

Fig. 2. Detail of the photosensitive section of the (A) 0.35 μm HVCMOS and (B) 0.16 μm BCD imagers, showing the five-by-five square SPAD array. (C) Front-end board (which is part of the complete detection system), hosting the image sensor and dedicated electronics.

C. Readout and Quenching Circuit

A SPAD is able to detect photons when its reverse bias voltage V_{BIAS} is raised above the breakdown value (which is around $V_{BD} = 25$ V for both technologies). The difference between bias and breakdown voltages is called excess-bias voltage ($V_{EX} = V_{BIAS} - V_{BD}$), and its value has a strong impact on SPAD performance as shown later. After each photon detection, the avalanche current has to be sensed by an external circuit, and the bias voltage must be reduced below breakdown as quickly as possible in order to *quench* the avalanche [9]. Correspondingly, a low-jitter output pulse is generated to mark the photon arrival time. After each avalanche quenching, the SPAD is kept disabled (i.e., biased below V_{BD}) for a few tens of nanoseconds (the so-called *hold-OFF* phase) in order to lower the probability of afterpulses [38]. Finally, the device is rearmed raising its bias voltage back to $V_{BD} + V_{EX}$.

Both imagers employ similar architectures for detector activation and avalanche readout. Each SPAD is connected to an independent active-quenching circuit based on a variable-load quenching circuit (VLQC) implementation [39], shown in the diagram of Fig. 3. When the SPAD is ready to detect photons, the transistor M_Q is weakly turned ON (showing a series resistance of few kilo-ohms), and the detector voltage is raised above breakdown. Transistors M_R and M_G are both turned OFF. When a photon is detected, the avalanche current flows through M_Q, and the resulting voltage drop is sensed by the control logic through the SENSE input. Then the control logic completely turns M_Q OFF, thereby increasing its impedance, and quickly turns M_G ON, which thus quenches the avalanche current by pulling up the anode voltage to V_{EX}. Correspondingly, a digital voltage pulse is generated at the EVENT OUT pin. After, the *hold-OFF* phase is enforced, keeping that pixel disabled for the entire dead time (T_D). To this aim, a common externally provided analog voltage (V_{HO}) is used to set the duration of T_D for all the pixels. At the end of this phase, M_G is turned OFF, M_Q is weakly turned ON again, and the transistor M_R is briefly activated in order to force back the anode voltage to ground and thus restoring the original SPAD bias conditions in less than 1 ns.

Additionally, a global enable input (GATE) allows simultaneous deactivation of all SPADs by connecting their anodes to the V_{EX} supply rail and thus biasing them below the breakdown voltage. Each individual pixel can also be turned ON/OFF via a configuration serial interface, allowing for exclusion of those SPADs whose outputs are not of interest for the measurement (thus preventing the increase of noise in neighbor pixels due to optical and electrical crosstalk) or which are too noisy. This serial interface is composed by a common clock signal (SCK) and a daisy-chained data line (SDI for input, SDO for output) passing through the 25 pixels.

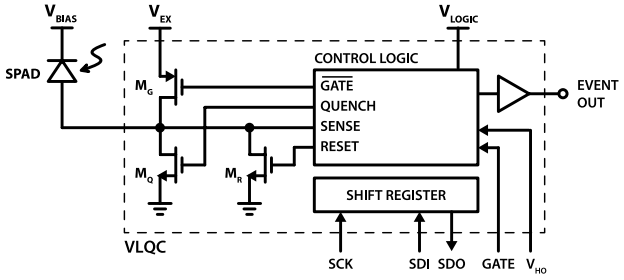

Fig. 3. Simplified circuit diagram of the in-pixel readout and quenching logic, based on a variable-load quenching circuit. Each pixel operates independently, marking photon detections by a voltage pulse at the output and subsequently enforcing the hold-off phase with programmable dead time T_D.

The front end makes use of thick-oxide transistors (M_Q, M_R, M_G) capable of withstanding the high excess bias of the SPADs, while the rest of the sensing circuitry is made with low-voltage transistors (3.3 V and 1.8 V for the HVCMOS and BCD chips, respectively). The readout and quenching circuitry are placed just outside the imaging area in order to maximize its fill factor.

D. Detection System Design

A complete and standalone detection system was developed in order to easily characterize the two image sensors and to exploit them in our ISM setup. It is based on two stacked printed circuit boards (PCBs). The upper one, called the *front-end board*, is shown in Fig. 2C and hosts (i) the detector; (ii) the bias voltage generator (implemented using a switching-mode boost converter followed by a linear voltage regulator); (iii) the dead-time control digital-to-analog converter (DAC); and (iv) the serial communication interface used to set the enabled/disabled status of each array pixel. The sensor chip is directly mounted onto the PCB and is electrically connected through direct bonding wires (chip-on-board mounting technique). A SM1-threaded mechanical mounting flange (*Thorlabs Inc.*) can be used to optically couple the system to the experimental setup.

Through a pair of high-density connectors, the *front-end board* is connected to a second PCB, called the *connection board*, which contains (i) the global power supply section, used to generate the system voltage rails (5.0 V, 3.3 V, and 1.8 V) starting from the common external 5 V–1 A supply; (ii) an 8-bit microcontroller, used to control and manage the entire system; and (iii) a set of 25 low-jitter buffers, able to drive 50 Ω impedance cables. Each buffered output, providing 3.3 V voltage pulses synchronous to photon detections, is connected to a coaxial cable with sub-miniature, type B (SMB) connectors. Cable connections for the serial interface control lines are also provided, allowing the user to independently enable each pixel.

3. EXPERIMENTAL CHARACTERIZATION

Before integration into the microscope, both SPAD arrays have been fully characterized in terms of detection efficiency, noise, afterpulsing probability, optical crosstalk, and timing jitter.

A. Photon Detection Efficiency

The photon detection efficiency (PDE) of the two imagers has been measured at a temperature of 300 K, over a wavelength range between 400 nm and 1000 nm, obtaining the results shown in Fig. 4A. The detector fabricated using the 0.35 μm HVCMOS technology (blue line) has a peak PDE of 40% at 430 nm, which drops below 10% starting from 750 nm, as already seen in similar devices reported in Ref. [18]. The 0.16 μm BCD sensor (red line) shows a substantially higher PDE, having a peak value of 65% around 500 nm and remaining above 20% in the entire range from 400 nm to around 750 nm. The excess bias voltage was set to 6 V and 5 V for the 0.35 μm HVCMOS and 0.16 μm BCD devices, respectively, as the optimal trade-off values between detection performance metrics. As expected, owing to the higher avalanche triggering probability of electrons [36], the 0.16 μm BCD SPAD

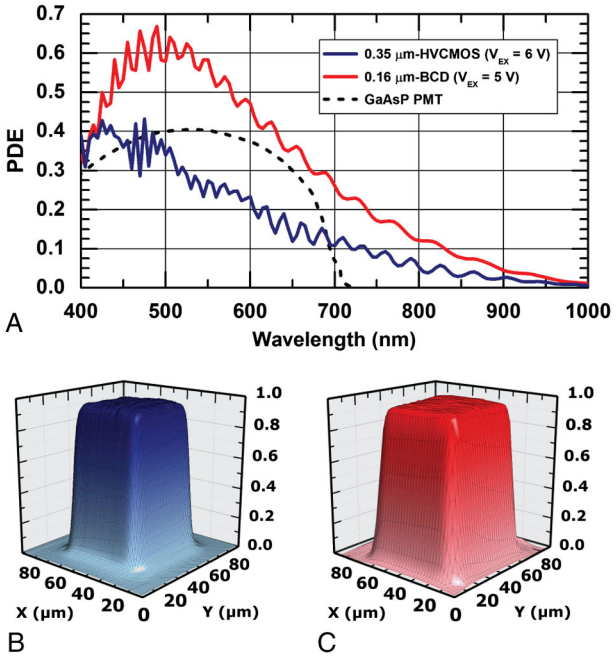

Fig. 4. (A) Photon detection efficiency of the 0.35 μm HVCMOS (blue curve) and 0.16 μm BCD (red curve) sensors, measured in the 400–1000 nm wavelength range. As a comparison, the PDE of a GaAsP PMT is also reported [40] (black dashed curve). (B) and (C) Normalized PDE uniformity inside the active area (for an individual pixel) of the 0.35 μm HVCMOS sensor and the 0.16 μm BCD sensor, respectively.

leads to a higher PDE compared to the 0.35 μm HVCMOS ones (where avalanches are triggered by holes) at all wavelengths. The interference ringing shown by both curves is due to the multiple dielectric layers and interfaces deposited on the chips during the back-end-of-line (BEoL) production phase. As a reference, Fig. 4A also includes the PDE of a GaAsP photomultiplier tube [40] (black dashed line), which is commonly used as detection element in laser scanning microscopy. The 0.16 μm BCD imager shows superior detection performance across the full measured wavelength range.

The uniformity of PDE inside the entire active area of a single pixel (the central one) was also measured, thanks to a laser-point scanning system, for both fabrication technologies. The resulting (normalized) 2D count maps are reported in Figs. 4B and 4C, showing extremely good uniformity and sharp drops outside active area borders, demonstrating a good electric field uniformity and the absence of edge peaking.

B. Noise

SPAD noise can be identified as all the electrical output pulses that are not due to photon detections. There are two major phenomena contributing to SPAD noise. The first one is related to avalanche ignitions triggered by carriers due to either thermal generation processes [41] or trap-assisted tunneling [42]. Such average rate is the SPAD dark-count rate (DCR). The second noise contribution is due to avalanches triggered by carriers that may get trapped by deep energy levels in the semiconductor during a previous avalanche and are released with a stochastic delay, eventually igniting a so-called *afterpulse* when the SPAD is rearmed [38]. This effect is quantified by the SPAD afterpulsing probability. Besides material quality, DCR depends also on device design and fabrication, operating temperature, and applied excess-bias voltage. On the other hand, afterpulses are strongly correlated to the detected signal and thus cause a nonlinear distortion of the acquired data. The afterpulsing effect is mitigated keeping the device OFF for a long time (dead time, T_D), typically tens of nanoseconds (from 20 to 200 ns), after each photon detection, and this indeed limits the maximum counting rate of each array element/pixel (with an asymptotical limit equal to $1/T_D$). Furthermore, since carrier detrapping is a thermally activated process, a decrease in the operating temperature of the device increases the afterpulsing probability, since longer detrapping times translate into more carriers released after the end of the dead time and thus originate more spurious avalanches [38].

Figure 5 shows the percentage distribution of DCR (related to individual pixels) for the two imagers herein described. The 0.35 μm HVCMOS SPADs (blue line) exhibit a DCR median of 200 counts per second (cps) at room temperature (300 K) with 6 V of excess-bias voltage, equivalent to 0.08 cps/μm^2. The 0.16 μm BCD SPADs have a higher DCR, with a median value of 2 kcps at 300 K and 5 V of excess-bias voltage, equivalent to 0.62 cps/μm^2. For this technology, due to the intrinsically higher DCR and the higher incidence of hot pixels, a proper testing and a careful selection of the device is required for each array to be used in ISM measurements. The yield of the two fabrication processes, which can be defined by the percentage of pixels having a DCR lower than 2 times the median value, is around 85% for the 0.35 μm HVCMOS and 67% for the 0.16 μm BCD.

It is worth remembering that the threshold DCR above which a pixel has to be considered a so-called *hot pixel* (i.e., having too-high noise to be usable) strongly depends on the application. In the case of ISM, thanks to the experience acquired during our measurements, we can set this threshold around 5 kcps (when imaging sufficiently bright samples). For other microscopy-related applications, a simple device selection may not be sufficient, forcing the implementation of an active cooling system (which, for silicon SPADs, guarantees approximately a decade in DCR decrease every 20 K of temperature reduction [41]), keeping in mind that there is usually a trade-off between DCR reduction and afterpulsing increase, when choosing the sensor operating temperature.

The afterpulsing probability at various dead times (T_D) is reported in Table 2. It has been measured by recording into a histogram the inter-arrival times between consecutive output pulses of an individual pixel. The contribution of simple DCR to this histogram can be fitted with an exponential decay at long inter-arrival

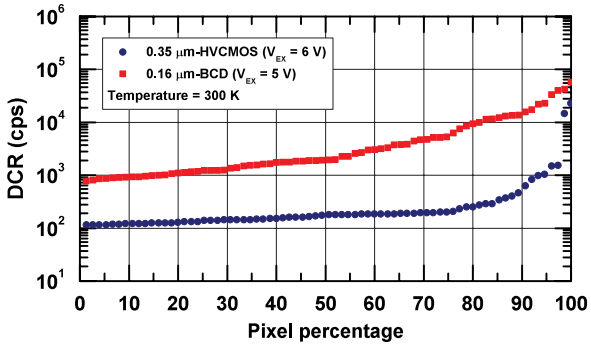

Fig. 5. Percentage distribution of dark-count rates (related to individual pixels) for the two imagers. The 0.35 μm HVCMOS SPADs (blue curve) have a DCR median of 200 cps at 300 K and 6 V of excess-bias voltage, while the 0.16 μm BCD ones (red curve) have a higher DCR median of 2 kcps at 300 K with 5 V excess-bias voltage.

Table 2. Afterpulsing Probability at Various Dead Times for 0.35 μm HVCMOS and 0.16 μm BCD SPAD Arrays

Dead Time (T_D)	0.35 μm HVCMOS	0.16 μm BCD
25 ns	14.70%	0.31%
50 ns	5.33%	0.25%
100 ns	2.37%	0.18%
200 ns	1.59%	0.09%

times and then subtracted from the experimental data in order to have only the contribution of avalanches due to afterpulses. Their probability is then computed as the integral sum of afterpulsing events, divided by the integral sum of the histogram itself (i.e., the total number of avalanches).

The afterpulsing performance of the 0.16 μm BCD is outstanding, showing only a 0.31% probability with T_D as short as 25 ns (equivalent to a maximum count rate of 40 Mcps per pixel). On the other hand, the minimum dead time needed to operate 0.35 μm HVCMOS SPADs with negligible afterpulsing effects (<3%) rises to 100 ns (equivalent to 10 Mcps of maximum count rate per pixel).

C. Temporal Response

The temporal response of a SPAD is very important for time-resolved applications, like fluorescence-lifetime ISM (FLISM), i.e., the combination of FLIM and ISM. Notably, FLISM, to the best of our knowledge, is the only effective super-resolution FLIM technique. The temporal response of a SPAD can be measured illuminating the device by means of a narrow pulsed laser (having a width of a few tens of picoseconds) and acquiring the distribution of photon arrival times by means of the time-correlated single-photon counting (TCSPC) technique [2]. A typical SPAD temporal response is composed of a narrow peak and a subsequent slower exponential tail [43]. The peak is essentially due to photons directly absorbed in the depleted region, where a photogenerated electron-hole pair is immediately separated and thus triggers the avalanche. Its FWHM gives a good indication of the detector timing resolution. The slower exponential tail is due to photons that have been absorbed within the device neutral regions. These carriers can diffuse and finally reach the high field region with some probability (many of them recombine before reaching it), eventually triggering a delayed avalanche with respect to the photon absorption time.

Figure 6A shows the single-pixel temporal response of the 0.35 μm HVCMOS imager: the blue curve is acquired with the remaining 24 pixels turned OFF, while the cyan curve is acquired with all the 25 pixels turned ON and illuminated. The characterization is performed using a pulsed diode laser at 850 nm, having less than 50 ps FWHM width and working at 1 MHz repetition rate (*Advanced Laser Diode System GmbH*). Photon arrival times were acquired using an SPC-630 TCSPC board (*Becker&Hickl GmbH*) with a time jitter of less than 8 ps FWHM. With all the remaining pixels turned OFF, the single-pixel temporal response width is 150 ps FWHM, with a fast exponential tail of 60 ps time constant. The measured temporal response is consistent across all 25 elements. When turning ON and illuminating the entire array, the single-pixel temporal response width rises to 200 ps FWHM, due to electrical crosstalk between switching signals (either inside the chip itself and through the front-end board).

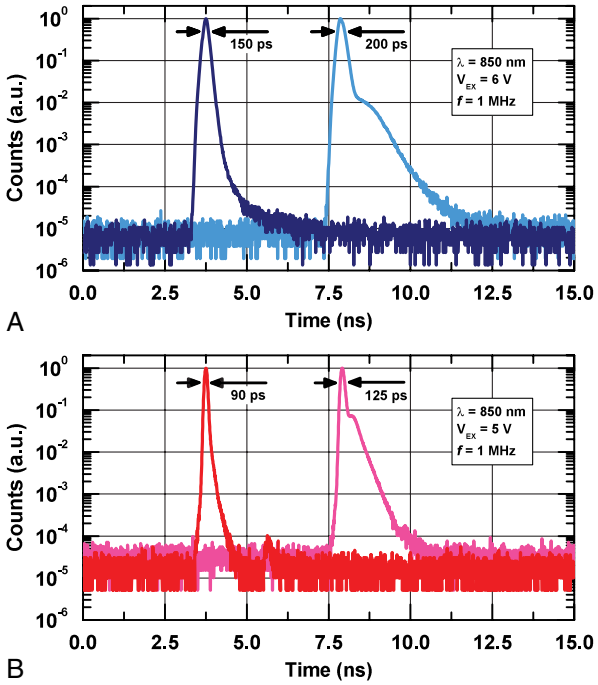

Fig. 6. Single-pixel temporal response of the (A) 0.35 μm HVCMOS and (B) 0.16 μm BCD imagers, measured using a 50 ps FWHM pulsed laser at 850 nm. The temporal responses have been measured with only one pixel turned ON (blue and red curves) and with all 25 pixels simultaneously ON and illuminated (cyan and magenta curves), showing the effect of optical crosstalk between adjacent pixels.

Furthermore, an additional bump appears after the main peak, due to photons generated by optical crosstalk between adjacent pixels (see Section 3.D). Figure 6B shows the temporal response of the 0.16 μm BCD sensor. With only one pixel turned ON (red curve), the response width is narrower than 90 ps FWHM, with an exponential tail time constant of 50 ps. With all 25 pixels turned ON (magenta curve), the response width slightly increases to 125 ps FWHM, and, also in this case, the effect of optical crosstalk becomes visible as an additional bump.

The worst-case (peak-to-peak) dispersion of the peak width is lower than 5 ps (of the FWHM) for both the devices when only one pixel is turned ON and increases up to a maximum of 30 ps having all 25 pixels enabled, due to the uneven effect of electrical crosstalk phenomena. Absolute time delays between the detection of a photon and the corresponding electrical output signal can have an offset in the order of a few hundreds of picosecond (which always remains constant and deterministic). Its main cause is not due to on-chip circuitry but rather to different propagation delays of output-driving buffers and PCB traces (and cables), which have slightly different lengths. This temporal offset is not an issue in practical measurements, since it can be easily estimated and compensated for in postprocessing.

D. Optical Crosstalk

Carriers flowing inside a SPAD during each avalanche can cause the emission of secondary photons due to hot-carrier relaxation phenomena. These secondary photons, propagating throughout the chip, can be absorbed into the active region of a nearby device, eventually causing spurious avalanches and degrading the measurement SNR. This effect is known as optical crosstalk

Table 3. Optical Crosstalk Probability between Adjacent Pixels (Orthogonally and Diagonally) for Both Imagers

Pixel Position	0.35 μm HVCMOS	0.16 μm BCD
First neighbors (orthogonal)	< 1.5%	< 5%
First neighbors (diagonal)	< 0.2%	< 0.3%

[44] and is influenced by several factors such as (i) device material and structure; (ii) distance between neighbor pixels (i.e., array pitch); (iii) intensity and duration of the avalanche current; and (iv) PDE of each pixel. The optical crosstalk probability can be quantified by measuring the temporal correlation between photon arrival times of two neighbor pixels, under weak ambient light. In absence of optical crosstalk phenomena, the inter-arrival time distribution (i.e., the distribution of time differences between a first event on one channel and a second event on the other channel, and vice versa) should follow an exponential decay (being a combination of two uncorrelated Poissonian processes). Crosstalk events create a variance from this theoretical trend and can be numerically quantified subtracting the latter from acquired data and normalizing.

Table 3 summarizes crosstalk probability values for the presented detectors, relative to first neighbor pixels, both in the orthogonal and diagonal directions. As anticipated, despite the relatively small probabilities (1.5% for the 0.35 μm HVCMOS and 5% for the 0.16 μm BCD sensors), the effect of optical crosstalk is clearly visible also looking at the single-pixel temporal response curves when all the pixels are turned ON and illuminated (Fig. 6, cyan and magenta curves). Notwithstanding the presence of deep oxide trenches, crosstalk probability is higher for the 0.16 μm BCD for multiple reasons: (i) smaller pixel separation, (ii) higher PDE, (iii) higher intensity of the avalanche current, and (iv) the multiplication region is deeper than the oxide trenches [45]. However, the relatively higher crosstalk probability of the 0.16 μm BCD sensor does not introduce any degradation in the spatial gain resolution (with respect to CLSM) obtained via ISM.

4. IMAGE-SCANNING MICROSCOPY EXPERIMENTS

Our imagers have been successfully integrated into ISM experiments to demonstrate the advantages of a SPAD-based detector and to compare the lower noise of a 0.35 μm HVCMOS device against the higher PDE of a 0.16 μm BCD one. Both SPAD arrays have been integrated into a custom CLSM, replacing its single-point detector, as described in detail in Refs. [26,46,47]. Output lines from the sensor array have been connected to an FPGA-based board (*NI-USB-7856R from National Instruments*) for counting photons detected in each laser spot position and for managing the entire microscope system (including the synchronization with scanning devices). Measurement control, data acquisition, and image reconstruction are performed using the *Carma* custom software [46,48].

Figure 7 shows images of tubulin filaments in a HeLa cell stained with Abberior STAR Red, where the 25 raw scanned images acquired from each independent pixel are processed using the adaptive pixel-reassignment (APR) method of [30], for obtaining the final ISM images. Pixel dwell time is 100 μs, and the imaged

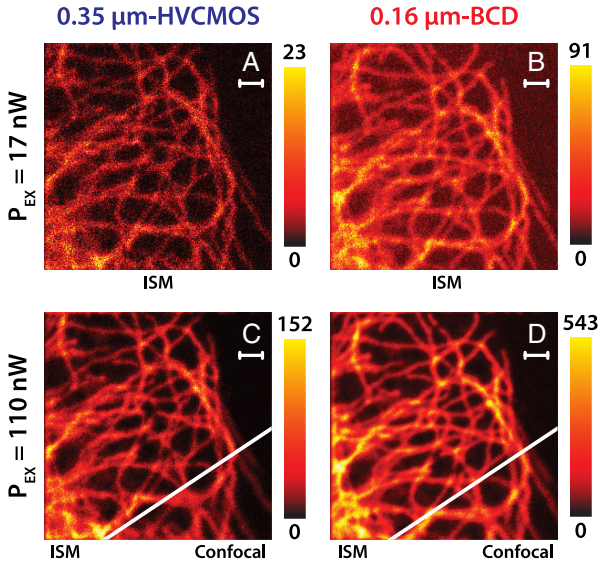

Fig. 7. ISM images of tubulin filaments stained with Abberior STAR Red, acquired using the two described five-by-five SPAD imagers (A, C for the 0.35 μm-HVCMOS and B, D for the 0.16 μm-BCD) and processed with the adaptive pixel reassignment (APR) method discussed in Ref. [30]. Pixel dwell time: 100 μs. Sample area: 10 × 10 μm^2 (scale bar: 1 μm). As a comparison, (C) and (D) also show the difference between ISM and standard confocal images (obtained simply summing together data from all 25 pixels).

sample area is equal to 10 × 10 μm^2. The photobleaching effect on sample is reduced by using a low laser excitation power (P_{EX}), at the expense of a small amount of fluorescence photons. Exacerbating this condition, as shown in Figs. 7A and 7B where $P_{EX} = 17$ nW (at 80 MHz repetition rate and 80 ps pulse width), the contrast is higher in the image obtained with the 0.35 μm HVCMOS sensor, owing to its lower DCR. However, the lower PDE of 0.35 μm HVCMOS SPADs may translate into the loss of some details of the sample structure in figure Fig. 7A with respect to Fig. 7B. Increasing the excitation power to $P_{EX} = 110$ nW translates into better image quality for both SPAD technologies [Figs. 7C and 7D]. However, the higher PDE and fill factor of the 0.16 μm BCD imager lead to a higher SNR.

Comparing the peak count values between ISM images in Fig. 7 and the corresponding images obtained considering only those photons detected by the central pixel (equivalent to an aperture size of approximatively 0.2 AU [46]), it is possible to evaluate the SNR boost achieved by ISM in comparison with closed-pinhole confocal imaging (at approximatively the same optical spatial resolution). Results are summarized in Table 4 and show an improvement ranging from a factor of 4.6× (for the 0.35 μm HVCMOS sensor) to a factor of 7.5× (for the 0.16 μm BCD one), similarly to current commercial ISM systems [35].

Resolution improvement in the images of Fig. 7 has been finally estimated, using the Fourier ring correlation (FRC) method [49]. Results are reported in Table 5, also compared to the resolution of the related confocal images, obtained summing together data from all 25 pixels and thus ensuring an almost equivalent image SNR. Since the FRC metric is sensitive to both optical resolution and SNR, and the two detectors were tested in the same imaging conditions, the improvement shown by the 0.16 μm BCD sensor compared to the 0.35 μm HVCMOS sensor is solely due to its higher PDE.

Table 4. Peak Counts Boost for the ISM Images of Fig. 7, Compared to Images Obtained Only from Photons Detected by the Central Pixel, Equivalent to a Pinhole Aperture of about 0.2 AU[a]

	0.35 μm HVCMOS		0.16 μm BCD	
Excitation Power (P_{EX})	Central Pixel (0.2 AU)	ISM	Central Pixel (0.2 AU)	ISM
17 nW	8	24 (3×)	18	91 (5.1×)
110 nW	33	152 (4.6×)	72	543 (7.5×)

[a](Which would be needed to obtain a comparable spatial super-resolution as explained in Ref. [46]).

Table 5. FRC-Based Resolution Values as a Function of the Excitation Power for the ISM Images of Fig. 7, Compared with the Related Confocal Images[a]

	0.35 μm HVCMOS		0.16 μm BCD	
Excitation Power (P_{EX})	Confocal	ISM	Confocal	ISM
17 nW	346 nm	271 nm	313 nm	257 nm
110 nW	314 nm	239 nm	251 nm	223 nm

[a]Obtained by simply summing together data from all 25 pixels.

5. DISCUSSION

The 0.35 μm HVCMOS was the earlier among the two imagers to be designed and fabricated, and it allowed us to successfully demonstrate for the first time the advantages of using asynchronous-readout SPAD arrays for ISM experiments [46]. Subsequently, we developed the 0.16 μm BCD SPADs, with better PDE, narrower temporal response, and lower afterpulsing probability, but with a higher noise.

Even if the final fill factor is substantially higher than SPAD imagers with in-pixel electronics, it could be further improved by a microlens array (MLA) mounted on top of the detector. Custom-shaped MLAs can be deposited directly on the chip by exploiting recently developed additive manufacturing techniques [50], with a theoretical equivalent fill factor of more than 78% (i.e., higher than the value theoretically achievable with circular lenses). For applications requiring wider arrays, the pixel number can be increased up to several tens of elements, but the final limitation would be related to chip size (due to the high number of independent output pads) and to signal integrity constraints inside the chip itself (due to the external positioning of the readout/quenching circuits needed in order to maximize the fill factor).

A. Advantages of an Asynchronous-Readout Array Detector

Large SPAD arrays with frame-based readout (mentioned in Section 1) are the natural choice for classical wide-field microscopy, since they allow simultaneously imaging of the entire sample without scanning it. However, there are several reasons why a smaller array with an asynchronous-readout architecture becomes the enabling sensor for advanced laser-scanning microscopy applications like ISM.

The first aspect is related to practical limits of current serial communication interfaces. It is possible to consider a hypothetical frame-based readout detector having the same performance of our five-by-five devices. The USB 3.0 communication protocol supports a theoretical readout speed up to 5 Gbit/s (equivalent to 5 bit/ns). Considering the simpler case of a frame readout time of 20 ns (i.e., slightly lower than the current minimum SPAD dead time) and a 1-bit counter per pixel (i.e., just marking one photon detection during each frame), it would be required to manage a data rate of 1.25 bit/ns, which would be sustainable by USB 3.0. However, in this scenario, the sensor will not be able to time-tag photons with a precision higher than the frame-rate period, which is unacceptable for the vast majority of time-resolved applications. To overcome such limitation, it would be necessary to add time-measurement circuitry inside each pixel (as usually done in larger SPAD arrays) and implement a frame-based readout of timing information. In this case, we can assume a built-in time-to-digital converter (TDC) having 20 ps of resolution and 20 ns of full-scale range (i.e., a 10-bit TDC). Keeping the same hypothetical frame rate of 1/(20 ns), the sensor will generate a data rate of 12.5 bit/ns, which will not be manageable using USB 3.0 without performing some data preprocessing. In some cases, the maximum frame rate and TDC performance could be relaxed (in nonresonant laser-scanning microscopy, the pixel dwell time is usually in the range of a few microseconds) but having on-chip TDCs translates in deciding their parameters *a priori* (i.e., resolution and number of bits), which thus renounces the flexibility intrinsically offered by having 25 independent output lines.

A second aspect is related to the synchronization of the sensor with the scanning architecture of the microscope. In this context, if the scanning architecture will act as a slave, the raster scanning process may not be effective. The complexity further increases when implementing a resonant scanning, where the pixel dwell time reduces to hundreds of nanoseconds and is not homogeneous. With an asynchronous-readout detector, the scanning synchronization is implemented within the control system of the microscope and thus does not restrict the universality of the system. Furthermore, new approaches for smart scanning are becoming popular [51], where the pixel dwell time is not deterministic but is decided in real time, which makes a frame-based readout architecture incompatible with these techniques.

B. Comparison with State-of-the-Art Detectors

As mentioned in the introduction, the *Airyscan* (*Carl Zeiss AG*) is currently the only commercial microscope implementing ISM. It employs a clever solution to overcome the speed limitation [kilohertz (kHz) frame rates] of conventional cameras, mimicking a 32-pixel bidimensional detector by using a hexagonally shaped bundle of optical fibers, coupled to a linear array of GaAsP PMTs [35]. This approach has been introduced mainly because of the lack of fast detection alternatives. Nowadays, microelectronic devices like SPADs are available as fast detectors and with high performance. It is not easy to directly compare specifications and measurements between our devices and the *Airyscan*. Generally speaking, GaAsP-based photocathodes lead to a lower PDE with respect to our BCD sensor, while no information about noise and crosstalk between channels is provided for the system described in Ref. [35]. Although results summarized in Table 4 confirm that our sensors achieve an SNR improvement similar to that of the *Airyscan*, in our opinion the latter has strong limitations due to the lack of time-resolving capabilities (time-resolved imaging and spectroscopy using *Airyscan* have not been demonstrated and never discussed), which comes almost for free with SPAD arrays.

Furthermore, the limited maximum readout speed of 1.28 μs per image [52] can hinder its combination with fast resonant scanners.

In Ref. [37], Antolovic *et al.* presented a 23-pixel SPAD array, designed in a 0.18 μm CMOS technology and targeted for ISM application. The overall sensor geometry is quite different with respect to ours, having round pixels with a radius of 5.85 μm, arranged hexagonally with a pixel pitch of 23 μm. Resulting fill factor is 23.5%, which translates into more than halving the collected photons compared to our implementations. SPAD parameters are somehow comparable, with our BCD detector being superior in terms of PDE, while [37] leading in regard to afterpulsing and crosstalk probability. Due to the implemented active cooling, the DCR of [37] is similar to our 0.35 μm HVCMOS device operating at room temperature. Nevertheless, we are working on a cooled version of our detectors that will show lower DCR. At the moment, a direct comparison between ISM imaging performance is not possible, since, to the best of our knowledge, no ISM measurements with the SPAD array presented in Ref. [37] have been reported in the literature.

In the more general context of confocal microscopy, another advantage of our detectors becomes important when imaging very bright samples at high scanning speed (and even more when using resonant scanners). Indeed, in this scenario, single-pixel SPAD-based detectors are disadvantaged with respect to their vacuum-based counterparts, due to the typical dead times, which are at least an order of magnitude higher than the PMT ones. In our current technologies, the best performance is reached by the BCD sensor, exhibiting a dead time as short as 25 ns with negligible afterpulsing probability. This limit is due to the intrinsic design of the electronics sketched in Fig. 3, while in a new design we are working to lower it down to 10 ns. However, when using the SPAD array detector, fluorescence photons from the sample are simultaneously spread over 25 different elements, providing an enormous boost to the sensor's dynamic range. Since those photons are distributed following the system's PSF, the achieved dynamic range will not be simply obtained multiplying by 25 the single-pixel one (most of the photons will impinge the central pixels), but stills turns out to be higher than faster the PMT's. We performed a simulation in this direction, considering a single-pixel PMT and a five-by-five SPAD array (pixel dead time of 25 ns) with a PSF-like photon arrival distribution [46]. Results show that the SPAD array's linear range (i.e., the photon flux interval for which the detector response is within 5% of the linear behavior) is increased by 7.2×, 3.7×, and 1.3× when compared to a PMT detector having dead times of 10, 5, and 2 ns, respectively. If we then consider an array of PMTs (like in the Zeiss Airyscan concept), a SPAD-based array returns to be slightly disadvantaged. Nevertheless, in this case one must consider also the issues related to data readout from PMT arrays (as mentioned above, *Airyscan* is limited to a readout speed of 1.28 μs per image), especially when dealing with resonant scanning systems.

Another alternative to solid-state arrays could be found in the so-called *multi-anode PMTs* [53]. However, the size of such detector becomes an important aspect to be considered. As an example, the *H7546A* (*Hamamatsu Photonics K.K*) of [53] is composed by a matrix of eight-by-eight PMTs, each one having dimensions of $2 \times 2\ \mathrm{mm}^2$. Indeed, thanks to the small size of a SPAD array, a relatively small magnification of the image plane is needed (i.e., the optimal projected detector size must be 1–1.5 AU, which translates into a magnification of around 450× with our objective lens), while bigger detector sizes would require much higher magnifications, which is not easy nor convenient to achieve practically.

C. Going Beyond ISM

We demonstrated that replacement of the standard single-point detector with our SPAD array module can easily and reversibly transform any existing CLSM into an image-scanning microscope, preserving all CLSM advantages (like the optical-sectioning capability) and without any need for prior calibrations. Moving a step forward, the single-photon timing capability of SPADs allowed us to add a further dimension to the measurements, making it possible to combine ISM with FLIM and thus enabling straightforward FLISM experiments [46], almost for free.

Remaining in the context of laser scanning microscopy, the ability of our SPAD array to image the excitation region (i.e., the detection volume) of the system can also improve the information content of many other advanced fluorescence microscopy techniques. An important application that could significantly benefit from our detectors is single-point fluorescence correlation spectroscopy (FCS), since they allow simultaneous measurement of the diffusion coefficients of a biomolecule for different detection volumes, giving access to the so-called FCS diffusion law [54]. In single-point FCS, a global analysis of the various intensity traces obtained by the different elements of the detector (i.e., by exploring the extra spatial information provided by the detector array) allows deciphering of the different diffusion modes of the investigated biomolecule [52]. In addition, remaining in the context of FCS measurements, the single-photon timing capability of SPAD arrays will also open the way to a synergic combination with fluorescence lifetime (FLCS), further improving the information content.

Outside microscopy, we can foresee other applications for this kind of sensor. These are not related to classical imaging (due to the small number of pixels), but rather aim to cleverly combine (spatially or temporally) the information simultaneously provided by each independent pixel. An example is background rejection in a single-pixel camera, for time-of-flight (ToF) measurements [55]. Here, by exploiting coincidence detection between different pixels, it is possible to identify events related to the (stronger) return signal from the target (which is related to the simultaneous activation of more than one pixel) with respect to photons related to uncorrelated ambient light (which have a lower probability to simultaneously trigger more than one element) [56]. A second example is related to diffuse optics and aims to noninvasively estimate the relative changes in blood perfusion by spatially measuring the autocorrelation function of laser speckles from coherent near-infrared light diffused by human tissues [57].

6. CONCLUSION

We designed, characterized, and evaluated two SPAD-based image sensors, specifically conceived for image-scanning microscopy applications. They are composed of 25 square pixels, having side dimensions of 50 μm with a maximum achievable fill factor higher than 50% (with further improvements made possible using microlenses). Each pixel integrates dedicated electronics for SPAD operation and is able to operate asynchronously from one another. Photon detections are marked with digital voltage pulses onto 25 independent output lines, with a time uncertainty lower than 200 ps (FWHM) at rates higher than $4 \cdot 10^7$ events/s. Depending on the fabrication technology, performance can be directed

towards high detection efficiency (more than 60% at 500 nm and about 30% at 650 nm) or low dark-count noise (200 cps at 25°C) with low optical crosstalk probability (below 2%). Both image sensors are hosted in a standalone detection system, which has been used to validate them in ISM experiments, showing superior improvements upon simple confocal microscopy and also enabling fluorescence-lifetime, two-photon excitation, and stimulated emission depletion ISM implementations [26,46,47].

Funding. Horizon 2020 Framework Programme (SOLUS, 731877); European Research Council (Bright Eyes, 818699).

Disclosures. M. B., F. V., M. C., G. T., P. B., A. D., G. V., and A. T.: Politecnico di Milano and Istituto Italiano di Tecnologia, WO/2019/145889 (P). M. C., S. P., P. B., A. D. and G. V.: Genoa Instruments, Italy (I).

REFERENCES

1. J. B. Pawley, ed., *Handbook of Biological Confocal Microscopy* (Springer, 1995).
2. W. Becker, ed., *Advanced Time-Correlated Single Photon Counting Applications* (Springer, 2015).
3. E. Haustein and P. Schwille, "Fluorescence correlation spectroscopy: novel variations of an established technique," Annu. Rev. Biophys. Biomol. Struct. **36**, 151–169 (2007).
4. S. W. Hell and J. Wichmann, "Breaking the diffraction resolution limit by stimulated emission-depletion fluorescence microscopy," Opt. Lett. **19**, 780–782 (1994).
5. G. Vicidomini, P. Bianchini, and A. Diaspro, "STED super-resolved microscopy," Nat. Methods **15**, 173–182 (2018).
6. C. B. Müller and J. Enderlein, "Image scanning microscopy," Phys. Rev. Lett. **104**, 198101 (2010).
7. I. Gregor and J. Enderlein, "Image scanning microscopy," Curr. Opin. Chem. Biol. **51**, 74–83 (2019).
8. P. P. Webb, R. J. McIntyre, and J. Conradi, "Properties of avalanche photodiodes," RCA Rev. **35**, 234–278 (1974).
9. F. Zappa, S. Tisa, A. Tosi, and S. Cova, "Principles and features of single-photon avalanche diode arrays," Sens. Actuators A **140**, 103–112 (2007).
10. A. Tosi, N. Calandri, M. Sanzaro, and F. Acerbi, "Low-noise, low-jitter, high detection efficiency InGaAs/InP single-photon avalanche diode," IEEE J. Sel. Top. Quantum Electron. **20**, 192–197 (2014).
11. H. Dautet, P. Deschamps, B. Dion, A. D. MacGregor, D. MacSween, R. J. McIntyre, C. Trottier, and P. P. Webb, "Photon counting techniques with silicon avalanche photodiodes," Appl. Opt. **32**, 3894–3900 (1993).
12. "SPCM-NIR single-photon detection module datasheet," 2020, http://www.excelitas.com.
13. M. Ghioni, S. Cova, A. Lacaita, and G. Ripamonti, "New silicon epitaxial avalanche diode for single-photon timing at room temperature," Electron. Lett. **24**, 1476–1477 (1988).
14. M. Ghioni, A. Gulinatti, I. Rech, F. Zappa, and S. Cova, "Progress in silicon single-photon avalanche diodes," IEEE J. of Sel. Top. in Quantum Electron. **13**, 852–862 (2007).
15. "PDM photon counting module datasheet," 2020, http://www.micro-photon-devices.com.
16. D. Bronzi, F. Villa, S. Tisa, A. Tosi, and F. Zappa, "SPAD figures of merit for photon-counting, photon-timing, and imaging applications: a review," IEEE Sens. J. **16**, 3–12 (2016).
17. R. K. Henderson, N. Johnston, F. M. D. Rocca, H. Chen, D. D.-U. Li, G. Hungerford, R. Hirsch, D. Mcloskey, P. Yip, and D. J. S. Birch, "A 192 × 128 time correlated SPAD image sensor in 40-nm CMOS technology," IEEE J. Solid-State Circuits **54**, 1907–1916 (2019).
18. F. Villa, D. Bronzi, Y. Zou, C. Scarcella, G. Boso, S. Tisa, A. Tosi, F. Zappa, D. Durini, S. Weyers, W. Brockherde, and U. Paschen, "CMOS SPADs with up to 500 μm diameter and 55% detection efficiency at 420 nm," J. Mod. Opt. **61**, 102–115 (2014).
19. R. K. Henderson, N. Johnston, S. W. Hutchings, I. Gyongy, T. A. Abbas, N. Dutton, M. Tyler, S. Chan, and J. Leach, "A 256 × 256 40 nm/90 nm CMOS 3D-stacked 120 dB dynamic-range reconfigurable time-resolved SPAD imager," in *IEEE International Solid-State Circuits Conference* (2019), pp. 106–108.
20. E. Charbon, C. Bruschini, and M. Lee, "3D-stacked CMOS SPAD image sensors: technology and applications," in *IEEE International Conference on Electronics Circuits and Systems* (2018), pp. 1–4.
21. K. Morimoto, A. Ardelean, M. L. Wu, A. Can Ulku, I. M. Antolovic, C. Bruschini, and E. Charbon, "Megapixel time-gated SPAD image sensor for 2D and 3D imaging applications," Optica **7**, 346–354 (2020).
22. D. Bronzi, F. Villa, S. Tisa, A. Tosi, F. Zappa, D. Durini, S. Weyers, and W. Brockherde, "100.000 frames/s 64 × 32 single-photon detector array for 2-D imaging and 3-D ranging," IEEE J. Sel. Top. Quantum Electron. **20**, 354–363 (2014).
23. F. Villa, R. Lussana, D. Bronzi, S. Tisa, A. Tosi, F. Zappa, A. Dalla Mora, D. Contini, D. Durini, S. Weyers, and W. Brockherde, "CMOS imager with 1024 SPADs and TDCs for single-photon timing and 3D time-of-flight," IEEE J. Sel. Top. Quantum Electron. **20**, 364–373 (2014).
24. D. Portaluppi, E. Conca, and F. Villa, "32 × 32 CMOS SPAD imager for gated imaging photon timing, and photon coincidence," IEEE J. Sel. Top. Quantum Electron. **24**, 1–6 (2018).
25. L. H. C. Braga, L. Gasparini, L. Grant, R. K. Henderson, N. Massari, M. Perenzoni, D. Stoppa, and R. Walker, "A fully digital 8 × 16 SiPM array for PET applications with per-pixel TDCs and real-time energy output," IEEE J. Solid-State Circuits **49**, 301–314 (2014).
26. G. Tortarolo, M. Castello, S. Koho, and G. Vicidomini, "Synergic combination of stimulated emission depletion microscopy with image scanning microscopy to reduce light dosage," bioRxiv 741389 (2020).
27. M. Bertero, C. De Mol, E. R. Pike, and J. G. Walker, "Resolution in diffraction-limited imaging, a singular value analysis IV. The case of uncertain localization or non-uniform illumination of the object," Opt. Acta **31**, 923–946 (1984).
28. C. J. R. Sheppard, "Super-resolution in confocal imaging," Optik **80**, 53–54 (1988).
29. C. J. R. Sheppard, S. B. Mehta, and R. Heintzmann, "Superresolution by image scanning microscopy using pixel reassignment," Opt. Lett. **38**, 2889–2892 (2013).
30. M. Castello, C. J. R. Sheppard, A. Diaspro, and G. Vicidomini, "Image scanning microscopy with a quadrant detector," Opt. Lett. **40**, 5355–5358 (2015).
31. G. M. R. De Luca, R. M. P. Breedijk, R. A. J. Brandt, C. H. C. Zeelenberg, B. E. de Jong, W. Timmermans, L. Nahidi Azar, R. A. Hoebe, S. Stallinga, and E. M. M. Manders, "Re-scan confocal microscopy: scanning twice for better resolution," Biomed. Opt. Express **4**, 2644–2656 (2013).
32. S. Roth, C. J. R. Sheppard, K. Wicker, and R. Heintzmann, "Optical photon reassignment microscopy (OPRA)," Opt. Nanosc. **2**, 5 (2013).
33. P. W. Winter, A. G. York, D. Dalle Nogare, M. Ingaramo, R. Christensen, A. Chitnis, G. H. Patterson, and H. Shroff, "Two-photon instant structured illumination microscopy improves the depth penetration of super-resolution imaging in thick scattering samples," Optica **1**, 181–191 (2014).
34. I. Gregor, M. Spiecker, R. Petrovsky, J. Großhans, R. Ros, and J. Enderlein, "Rapid nonlinear image scanning microscopy," Nat. Methods **14**, 1087–1089 (2017).
35. J. Huff, "The Airyscan detector from ZEISS: confocal imaging with improved signal-to-noise ratio and super-resolution," Nat. Methods **12**, i–ii (2015).
36. M. Sanzaro, P. Gattari, F. Villa, G. Croce, and F. Zappa, "Single-photon avalanche diodes in a 0.16 μm BCD technology with sharp timing response and red-enhanced sensitivity," IEEE J. Sel. Top. Quantum Electron. **24**, 1–9 (2018).
37. I. M. Antolovic, C. Bruschini, and E. Charbon, "Dynamic range extension for photon counting arrays," Opt. Express **26**, 22234–22248 (2018).
38. S. Cova, A. Lacaita, and G. Ripamonti, "Trapping phenomena in avalanche photodiodes on nanosecond scale," IEEE Electron Device Lett. **12**, 685–687 (1991).
39. D. Bronzi, S. Tisa, F. Villa, S. Bellisai, A. Tosi, and F. Zappa, "Fast sensing and quenching of CMOS SPADs for minimal afterpulsing effects," IEEE Photon. Technol. Lett. **25**, 776–779 (2013).
40. "PMT2101 amplified photomultiplier tube module datasheet," 2020, http://www.thorlabs.com.
41. A. S. Grove, ed., *Physics and Technology of Semiconductor Devices* (Wiley, 1967).

42. A. Migdall, S. V. Polyakov, J. Fan, and J. C. Bienfang, "Single-photon generation and detection," in *Experimental Methods in the Physical Sciences* (Academic, 2013), Vol. **45**.
43. S. Cova, G. Ripamonti, and A. Lacaita, "Avalanche semiconductor detector for single optical photons with a time resolution of 60 ps," Nucl. Instrum. Methods **A253**, 482–487 (1987).
44. I. Rech, A. Ingargiola, R. Spinelli, I. Labanca, S. Marangoni, M. Ghioni, and S. Cova, "Optical crosstalk in single photon avalanche diode arrays: a new complete model," Opt. Express **16**, 8381–8394 (2008).
45. M. Sanzaro, F. Signorelli, P. Gattari, A. Tosi, and F. Zappa, "0.16 μm—BCD silicon photomultipliers with sharp timing response and reduced correlated noise," Sensors **18**, 3763 (2018).
46. M. Castello, G. Tortarolo, M. Buttafava, T. Deguchi, F. Villa, S. Koho, L. Pesce, M. Oneto, S. Pelicci, L. Lanzanó, P. Bianchini, C. J. R. Sheppard, A. Diaspro, A. Tosi, and G. Vicidomini, "A robust and versatile platform for image scanning microscopy enabling super-resolution FLIM," Nat. Methods **16**, 175–178 (2019).
47. S. V. Koho, E. Slenders, G. Tortarolo, M. Castello, M. Buttafava, F. Villa, E. Tcarenkova, M. Ameloot, P. Bianchini, C. J. R. Sheppard, A. Diaspro, A. Tosi, and G. Vicidomini, "Two-photon image-scanning microscopy with SPAD array and blind image reconstruction," Biomed. Opt. Express **11**, 2905–2924 (2020).
48. M. Castello, G. Tortarolo, I. Coto Hernández, T. Deguchi, A. Diaspro, and G. Vicidomini, "Removal of anti-Stokes emission background in STED microscopy by FPGA-based synchronous detection," Rev. Sci. Instrum. **88**, 053701 (2017).
49. G. Tortarolo, M. Castello, A. Diaspro, S. Koho, and G. Vicidomini, "Evaluating image resolution in stimulated emission depletion microscopy," Optica **5**, 32–35 (2018).
50. S. Surdo, R. Carzino, A. Diaspro, and M. Duocastella, "Single-shot laser additive manufacturing of high fill-factor microlens arrays," Adv. Opt. Mater. **6**, 1701190 (2018).
51. J. Dreier, M. Castello, G. Coceano, R. Cáceres, J. Plastino, G. Vicidomini, and I. Testa, "Smart scanning for low-illumination and fast RESOLFT nanoscopy in vivo," Nat. Commun. **10**, 556 (2019).
52. L. Scipioni, L. Lanzanó, A. Diaspro, and E. Gratton, "Comprehensive correlation analysis for super-resolution dynamic fingerprinting of cellular compartments using the Zeiss Airyscan detector," Nat. Commun. **9**, 5120 (2018).
53. "H7546A multianode photomultiplier tube assembly datasheet," 2020, http://www.hamamatsu.com.
54. L. Wawrezinieck, H. Rigneault, D. Marguet, and P. F. Lenne, "Fluorescence correlation spectroscopy diffusion laws to probe the submicron cell membrane organization," Biophys. J. **89**, 4029–4042 (2005).
55. G. Musarra, A. Lyons, E. Conca, Y. Altmann, F. Villa, F. Zappa, M. J. Padgett, and D. Faccio, "Non-line-of-sight three-dimensional imaging with a single-pixel camera," Phys. Rev. Appl. **12**, 011002 (2019).
56. M. Perenzoni, D. Perenzoni, and D. Stoppa, "A 64 × 64-pixels digital silicon photomultiplier direct TOF sensor with 100-MPhotons/s/pixel background rejection and imaging/altimeter mode with 0.14% precision up to 6 km for spacecraft navigation and landing," IEEE J. Solid-State Circuits **52**, 151–160 (2017).
57. J. D. Johansson, D. Portaluppi, M. Buttafava, and F. Villa, "A multipixel diffuse correlation spectroscopy system based on a single photon avalanche diode array," J. Biophoton. **12**, e201900091 (2019).